Research Square

Preprints are preliminary reports that have not undergone peer review.
They should not be considered conclusive, used to inform clinical practice,
or referenced by the media as validated information.

Hexplorer: A Biomimetic Amphibious Hexapod Robot for Locomotion in Terrestrial and Aquatic Environments

Ziliang Chen
Southeast University
Jiahong He
hejiahong@seu.edu.cn
Southeast University
Bingtuan Gao
Southeast University
Linlin Zhong
Southeast University

Research Article

Keywords: amphibious robot, hexapod robot, rigid–flexible leg–fin, multimodal locomotion, central pattern generator, actuator reuse

Posted Date: October 30th, 2026

DOI: https://doi.org/10.21203/rs.3.rs-11200344/v1

License: This work is licensed under a Creative Commons Attribution 4.0 International License.
Read Full License

Additional Declarations: No competing interests reported.

Hexplorer: A Biomimetic Amphibious Hexapod Robot for Locomotion in Terrestrial and Aquatic Environments

Ziliang Chen[1], Jiahong He[1*], Bingtuan Gao[1], Linlin Zhong[1]

[1*]School of Electrical Engineering, Southeast University, Nanjing, 210096, China.

*Corresponding author(s). E-mail(s): hejiahong@seu.edu.cn;
Contributing authors: 230269447@seu.edu.cn; gaobingtuan@seu.edu.cn; linlin@seu.edu.cn;

Abstract

For locomotion in both terrestrial and aquatic environments, amphibious robots require appendages that can bear loads on land and generate propulsion in water. This paper presents the design and experimental evaluation of Hexplorer, a hexapod robot equipped with six identical leg–fin units that provide a total of twelve actuated degrees of freedom. Each unit combines a vertical prismatic hip with a rotary leg–fin comprising a rigid fan-shaped contact frame and a compliant fin. The mechanical parameters of the leg–fin units are jointly optimized to improve adaptability during terrestrial locomotion. A central pattern generator (CPG)-based gait generation algorithm coordinates the twelve joints and automatically switches between crawling and swimming gaits by changing the gait mapping. In experiments, the robot traveled at 0.0208 m/s on flat indoor ground, 0.0250 m/s on outdoor unstructured ground, 0.1250 m/s at the water surface, and 0.0357 m/s on an underwater substrate. Using the same appendages and actuators, Hexplorer achieves coverage of four locomotion scenarios.

Keywords: amphibious robot, hexapod robot, rigid–flexible leg–fin, multimodal locomotion, central pattern generator, actuator reuse
JIRS categories: (3) and (6)

1 Introduction

Robots operating at the land–water interface can assist with sediment sampling on tidal flats [1] and near-seabed observation [2]. Their appendages must accommodate different mechanical demands. On land, they transmit support forces, generate traction, and clear the ground during recovery. Swimming depends on appendage area, orientation,

deformation, and stroke, while underwater bottom locomotion requires contact with the substrate under buoyancy. Integrating these functions remains a challenge in amphibious robot design and control [3, 4]. Hybrid mechanisms allow hardware to serve more than one environment [5], but require a suitable combination of load-bearing structure, fluid-interaction surfaces, and coordinated motion.

Biological fins provide examples of combined support and propulsion. Epaulette sharks use paired fins and body bending to move along the bottom [6]. Hale et al. distinguish regionalized pectoral fins, with different regions for substrate contact and swimming, from generalized fins that use a broader surface for contact [7]. Mudskippers also use their pectoral fins for terrestrial support and propulsion despite limited proximal mobility; distal flexibility may help accommodate this restriction [8]. These observations motivate placing load-bearing and compliant regions within the same robotic appendage.

Existing amphibious robots combine locomotor functions in several ways. AmphiRobot-II integrates wheels, propellers, and fins through a swivel device [9]. A track–fin robot drives tracks and undulating fins simultaneously, allowing each to act in its respective medium [10]. Paddle-wheeled legs combine ground locomotion and aquatic propulsion with a switching mechanism and torque-based medium recognition [11]. Other designs use the same component for both functions: SHOALBOT uses propeller-legs for ground or seabed running and swimming [12], and cycloidal modules operate as underwater propellers and terrestrial blade wheels [13]. AmphiHFW couples an undulating fin and a leg–wheel structure through a single actuator [14]. These mechanisms differ in their transmissions, contact geometry, and available strokes.

Changing appendage morphology or stiffness provides another route to reconciling mechanical demands. AmphiHex-I uses transformable flipper-legs to combine terrestrial locomotion with aquatic operation [15]. Chelonian-inspired morphing limbs use variable-stiffness material and pneumatic actuation to change between a load-bearing leg and a hydrodynamic flipper [16], and adaptive morphogenesis extends this approach to coordinated changes in limb shape and gait at the robot level [17]. The energetic cost of transformation is itself a design consideration: Ramirez et al. address it using pressure-responsive kirigami laminar jamming [18]. Recent origami limbs use a controlled folding path to alternate between a cylindrical support configuration and a planar paddling configuration [19]. Soft pneumatic robots further demonstrate that compliant bodies can produce multiple terrestrial and aquatic behaviors, although the reported system relies on a tethered pneumatic supply [20]. These approaches expand the range of useful shapes and motions, while making shape control, stiffness regulation, or pressure delivery part of the overall system design.

Passive compliance allows an appendage to retain its basic structure across environments. AmphiHex-II combines a rigid fan-shaped frame and a flexible flipper, with one rotary actuator per leg and manually positioned sliders for stiffness adjustment [21]. FLHex uses a passive flapped paddle on a curved leg to create asymmetric hydrodynamic interaction during oscillation [22]. A tensegrity mudskipper robot similarly uses pectoral fins with asymmetric stiffness during power and recovery strokes [23]. HERO-BLUE combines fins containing passive joints with a spine and an undulating fin for underwater swimming, walking, and crawling [24]. These designs motivate examining

how active joints position a leg–fin and how its rigid and compliant parts transmit loads in each mode.

Gait generation must coordinate the available motions of the mechanism. Pectoral–caudal fin coordination has improved the maneuverability of a mudskipper-inspired robot [25], while a recent amphibious turtle robot combines three-degree-of-freedom flippers with visual–tactile terrain classification and gait adaptation [26]. For rhythmic joint coordination, central pattern generators (CPGs) are widely used. Hopf networks have been applied to amphibious hexapods [21] and combined with fuzzy heading control for arc-shaped blade legs [27]. Applying them to a prismatic–rotary appendage requires joint mappings and interleg phase relations suited to its motion.

We propose Hexplorer, a hexapod with six identical two-degree-of-freedom (2-DOF) leg–fin units for terrestrial crawling, water-surface swimming, and underwater bottom crawling. Each unit combines a vertical prismatic hip with a rotary rigid–flexible leg–fin. The rigid fan-shaped frame bears substrate loads, and the compliant thermoplastic polyurethane (TPU) fin interacts with water. Compared with the single rotary joint of AmphiHex-II [21], the additional prismatic joint allows elevation to be controlled independently of leg–fin rotation. The appendage structure remains unchanged across modes.

The main contributions are:

1. A 2-DOF leg–fin unit combines a prismatic hip, a rigid contact frame, and a compliant fin. Six identical units provide terrestrial and aquatic locomotion without separate wheels, tracks, or propellers. Geometric parameter optimization balances contact sweep and radial reach within the available interleg spacing.

2. A Hopf-based CPG gait generation algorithm is designed for the Hexplorer prototype to coordinate its twelve joints through crawling and swimming mappings, interleg phase relations, and handheld direction input.

3. Experiments demonstrate that the prototype uses the same appendages and actuators to move in four scenarios: flat ground, outdoor unstructured ground, the water surface, and an underwater substrate.

2 Robot and Appendage Design

2.1 Overall architecture and amphibious appendage

Hexplorer combines a rigid torso with six identical leg–fin units, arranged three per side. Each unit has a vertically translating prismatic hip and a rotary leg joint, providing twelve actuated degrees of freedom in total. The prototype has a mass of 7.2 kg and a nominal envelope of 400 × 350 × 300 mm (length × width × height). Figure 1A shows the assembled mechanism and its dimensioned views.

The single-appendage drive layout in Fig. 1B identifies the rotary output shaft and the guided sliding hip. A rack-and-pinion transmission converts hip-motor rotation into vertical travel, while the rotary drive turns the leg–fin about its output shaft. During crawling, coordinated translation and rotation lift the appendage, recover it, establish contact, and generate the support stroke. During water-surface swimming, the hip remains at a selected setting and the rotary joint oscillates the appendage.

Thus, the prismatic joint controls elevation independently of the rotary stroke, within the limits of the guide and transmission.

The distal amphibious mechanism comprises two functional parts (Fig. 1B). A rigid fan-shaped frame with an anti-slip contact edge transfers substrate loads to the rotary shaft and torso during terrestrial and underwater bottom crawling. A flexible thermoplastic polyurethane (TPU) fin provides the surface that interacts with water during swimming. Both parts remain attached in each mode, so locomotion does not require an exchange of appendages or separate propellers. Fin compliance is passive; the mechanism does not actively change stiffness.

At a fixed leg angle, the prismatic hip changes endpoint height without horizontal displacement in the rigid-body model. This permits vertical recovery within a compact lateral envelope. The added guide and rack-and-pinion transmission introduce friction and guide loads that must be considered when sizing the hip drive.

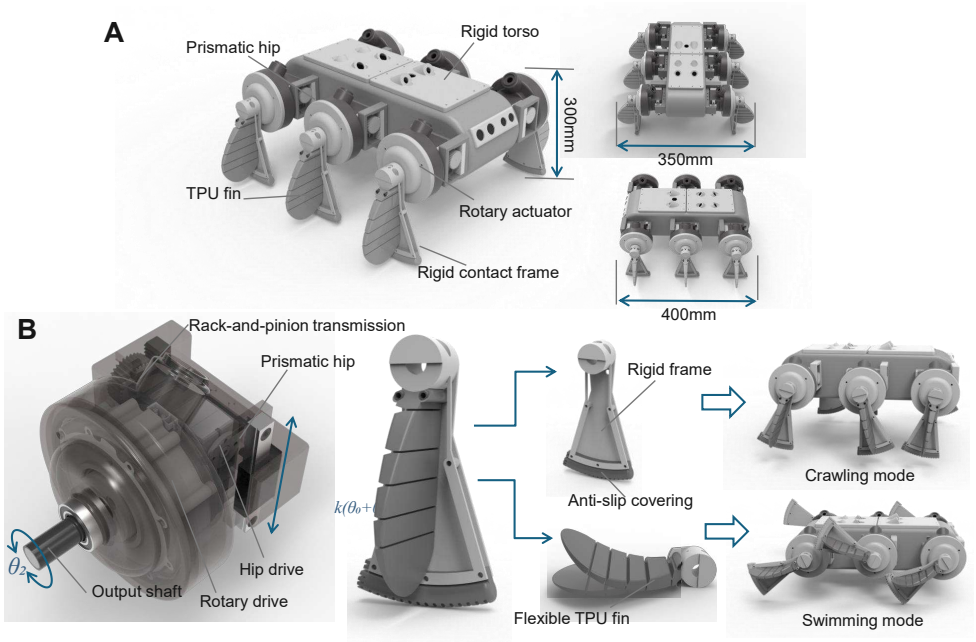


Fig. 1 Overall architecture and functional allocation of Hexplorer. (A) Robot assembly and dimensioned views, with a nominal length, width, and height of 400, 350, and 300 mm. (B) Single-appendage drive layout identifying the rotary output shaft, guided prismatic hip, and rack-and-pinion transmission. The rigid contact frame and anti-slip edge support crawling; the flexible TPU fin provides the aquatic interaction surface during swimming. Both parts remain attached in each mode.

2.2 Single-appendage kinematics

Figure 2A defines the torso frame {1}, hip frame {2}, and rotary leg frame {3}; Fig. 2B shows their sagittal projection. The rear endpoint of the rigid fan frame is denoted by P. The hip offset is l_{H}, and the effective leg length is $l_{\mathrm{L}} = R$. In the mechanical

notation, θ_1 denotes hip-drive rotation, θ_0 its initial mechanical offset, and θ_2 leg-joint rotation. The hip translation is $k_t(\theta_0 + \theta_1)$, where $k_t = 0.04/(2\pi) \approx 0.00637$ m/rad: a 2π rad rotation of the hip drive produces 4 cm of prismatic travel. The model treats the frame as rigid and does not represent flexible-fin deformation.

The homogeneous transformations are

$$T_{12} = \begin{bmatrix} R_{12} & p_{12} \\ 0_{1\times3} & 1 \end{bmatrix}, \qquad T_{23} = \begin{bmatrix} R_{23} & p_{23} \\ 0_{1\times3} & 1 \end{bmatrix}. \tag{1}$$

For the frame origins shown in Fig. 2A, the fixed lateral offset belongs to the translation between the hip and rotary frames. The corresponding transformations and endpoint vector are

$$\begin{aligned} T_{12} &= \begin{bmatrix} 1 & 0 & 0 & 0 \\ 0 & 1 & 0 & 0 \\ 0 & 0 & 1 & k_t(\theta_0+\theta_1) \\ 0 & 0 & 0 & 1 \end{bmatrix}, \\ T_{23} &= \begin{bmatrix} \cos\theta_2 & 0 & \sin\theta_2 & 0 \\ 0 & 1 & 0 & l_H \\ -\sin\theta_2 & 0 & \cos\theta_2 & 0 \\ 0 & 0 & 0 & 1 \end{bmatrix}, \qquad P_3 = \begin{bmatrix} 0 \\ 0 \\ -l_L \end{bmatrix}. \end{aligned} \tag{2}$$

Multiplying the transformations gives

$$\begin{bmatrix} P_1 \\ 1 \end{bmatrix} = T_{12}T_{23}\begin{bmatrix} P_3 \\ 1 \end{bmatrix} = \begin{bmatrix} x_P \\ y_P \\ z_P \\ 1 \end{bmatrix} = \begin{bmatrix} -l_L \sin\theta_2 \\ l_H \\ -l_L\cos\theta_2 + k_t(\theta_0+\theta_1) \\ 1 \end{bmatrix}. \tag{3}$$

The fixed lateral coordinate is $y_P = l_H$. In the sagittal projection, x_P and z_P denote the same torso-referenced components as x_P and z_P. Including the hip translation, the planar relation is

$$\begin{bmatrix} x_P \\ z_P \end{bmatrix} = \begin{bmatrix} \cos\theta_2 & \sin\theta_2 \\ -\sin\theta_2 & \cos\theta_2 \end{bmatrix}\begin{bmatrix} 0 \\ -l_L \end{bmatrix} + \begin{bmatrix} 0 \\ k_t(\theta_0+\theta_1) \end{bmatrix}. \tag{4}$$

The vertical relation and its rearrangement for the hip drive are

$$l_L\cos\theta_2 + z_P = k_t(\theta_0+\theta_1). \tag{5}$$

$$\theta_1 = \frac{l_L\cos\theta_2 + z_P}{k_t} - \theta_0. \tag{6}$$

For the branch with $-\pi/2 \le \theta_2 \le \pi/2$, the inverse solution is

$$\begin{cases} \theta_1 = \dfrac{l_L}{k_t}\cos\left[\arcsin\left(-\dfrac{x_P}{l_L}\right)\right] + \dfrac{z_P}{k_t} - \theta_0, \\ \theta_2 = \arcsin\left(-\dfrac{x_P}{l_L}\right). \end{cases} \tag{7}$$

The inverse solution requires $|x_P| \le l_L$ and must satisfy the hip-travel and rotary-joint limits.

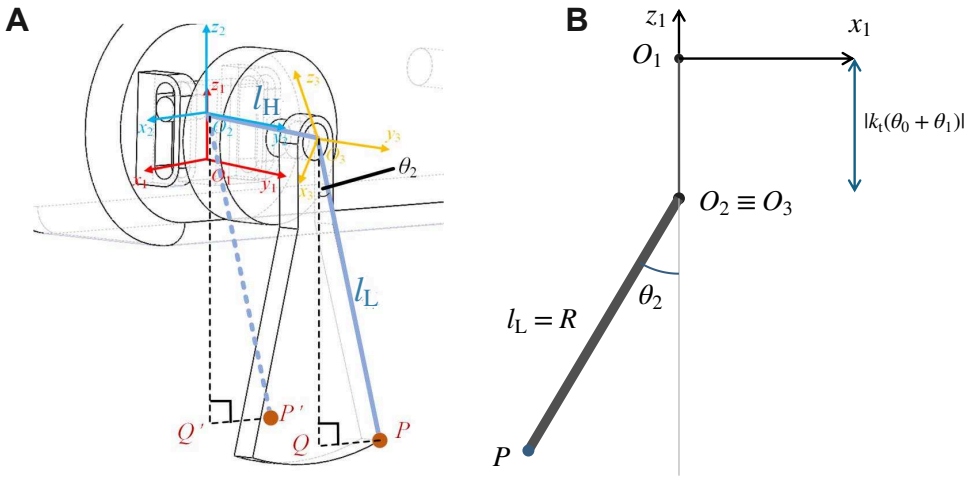


Fig. 2 Single-appendage kinematics. (A) Spatial arrangement of the torso, hip, and rotary frames, with hip offset l_{H}, leg length l_{L}, leg angle θ_2, and endpoint P. (B) Sagittal projection used for the forward and inverse relations. The physical origins O_2 and O_3 are separated laterally by l_{H} and coincide in this projection. The vertical dimension denotes the magnitude of $k_{\mathrm{t}}(\theta_0 + \theta_1)$.

At fixed θ_2, varying θ_1 changes only endpoint height; varying θ_2 traces a rotary arc. Assessment of the spacing between two adjacent leg–fin units must also account for the swept volume of the frame, actuator housing, and flexible fin.

2.3 Fan geometry and adjacent-appendage clearance

The equivalent radius R and central angle α determine the extent of the rigid fan-shaped contact frame. A larger radius extends the reach of the leg–fin, whereas a longer sector arc provides a larger potential contact sweep. Both dimensions are constrained by interference between neighboring appendages (Fig. 3A). In the planar construction in Fig. 3B, l_1 is the central coupling radius and l_2 is the radial extent of the sector support, giving $R = l_1 + l_2$. The body layout fixes the adjacent hip spacing at $x = x_0 = 120$ mm. With $l_1 = 10$ mm, the radius and angle are selected jointly subject to

$$\begin{cases} R\sin\alpha \le 0.5x_0 + l_1, \\ l_1 \le R \le x_0 + l_1, \\ 0 \le \alpha \le 0.5\pi. \end{cases} \tag{8}$$

The two geometric objectives are to maximize the sector arc length $S = R\alpha$ and the radius R, representing potential contact sweep and radial reach, respectively; α is expressed in radians. The normalization references S_{ref} and R_{ref} are the independently attainable maxima of these objectives over the feasible region. Let $c = 0.5x_0 + l_1 = 70$ mm. The radius bound gives $R_{\mathrm{ref}} = x_0 + l_1 = 130$ mm. On the angular constraint boundary, $S = c\alpha/\sin\alpha$ increases with α up to 0.5π, giving $S_{\mathrm{ref}} = 0.5\pi c$ at $R = c$ and

$\alpha = 0.5\pi$. The two reference maxima occur at different designs. An ideal-point criterion selects a compromise by minimizing the weighted sum of squared relative shortfalls:

$$J(R, \alpha, \kappa) = (1 - \kappa)\left(1 - \frac{R\alpha}{S_{\text{ref}}}\right)^2 + \kappa\left(1 - \frac{R}{R_{\text{ref}}}\right)^2, \quad 0 < \kappa < 1. \tag{9}$$

Here, κ is a prescribed weight controlling the emphasis on radius. We set $\kappa = 0.5$ to weight the two squared relative shortfalls equally.

For any fixed radius, increasing α improves the arc-length objective until the angular bound is reached. Designs with $R < c$ are dominated by $(R, \alpha) = (c, 0.5\pi)$, which offers both a larger radius and a longer arc. The Pareto candidates therefore satisfy

$$\alpha(R) = \arcsin\left(\frac{c}{R}\right), \qquad c \le R \le R_{\text{ref}}. \tag{10}$$

Along this boundary, $R\alpha(R)$ decreases as R increases, exposing the trade-off between contact sweep and reach. Substituting Eq. 10 into Eq. 9 reduces the joint selection to

$$R^* = \underset{c \le R \le R_{\text{ref}}}{\arg\min}\ J\Big(R, \arcsin\frac{c}{R}, 0.5\Big), \qquad \alpha^* = \arcsin\frac{c}{R^*}. \tag{11}$$

A uniform radius scan with bounded scalar refinement and endpoint comparison gives $R^* = 126.05$ mm and $\alpha^* = 33.73°$ (Fig. 3C). The angular constraint is active at the optimum. Taking fabrication tolerances into account, the final experimental prototype was built with $R = 130$ mm and $\alpha = 34°$.

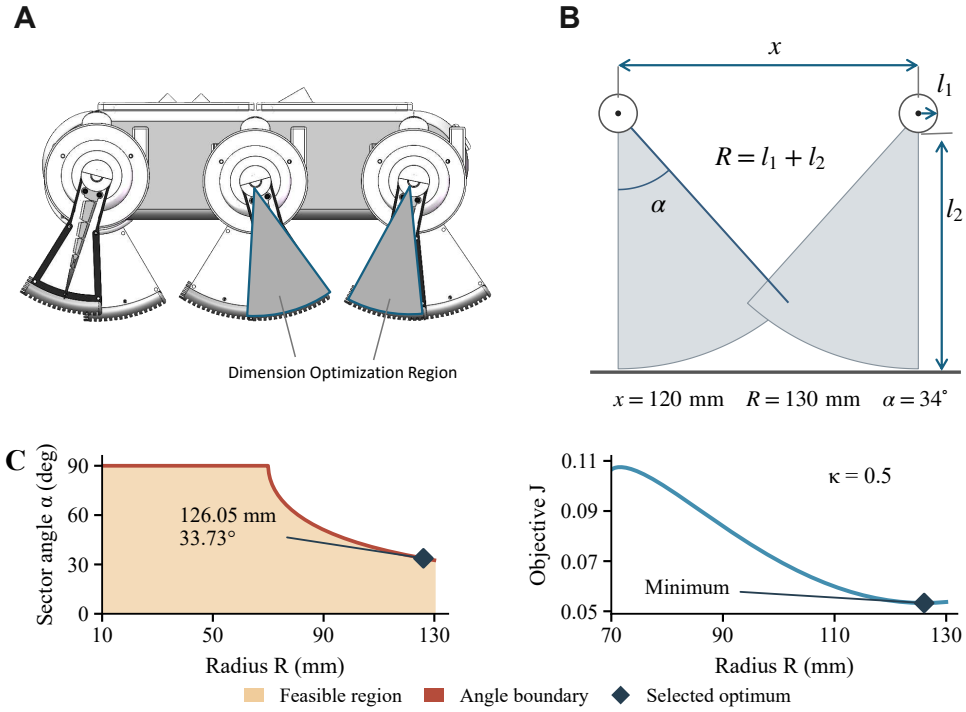


Fig. 3 Fan geometry and ideal-point optimization. (A) Adjacent leg–fin sectors during rotation. (B) Planar geometry with $R = l_1 + l_2$; the displayed dimensions are nominal prototype values. (C) Optimization at $x = 120$ mm and $l_1 = 10$ mm. Left: the feasible region and angular boundary. Right: the objective along the Pareto boundary ($\kappa = 0.5$). Diamonds mark the model optimum, $R^* = 126.05$ mm and $\alpha^* = 33.73°$.

2.4 Waterproof actuation and buoyancy-compartment integration

Figure 4A shows the integrated actuator package in exploded form, and Fig. 4B shows the rotary-drive and hip-drive cross-sections. The rotary leg joint uses a 24 V brushless DC motor with a planetary reducer (320 g per unit), while the hip drive uses a 12 V geared motor (30 g per unit). The hip pinion engages the rack, and the guide constrains the translating assembly. Table 1 summarizes the prototype specifications.

Static housing interfaces are sealed with compressed nitrile O-rings, and circuit boards are potted in epoxy. PTFE lip seals contact the rotating shafts, which are supported by bearings. Figure 4 shows the positions of the seals and bearings relative to the two drives.

The torso cross-section in Fig. 4C locates the adjustable-displacement buoyancy compartments within the lower body, above the appendage attachments. These compartments provide the buoyancy adjustment used to configure surface floating or

Table 1 Mechanical and material specifications

Parameter	Specification
Appendages / active DOFs	6 / 12
DOFs per appendage	1 prismatic + 1 rotary
Prototype mass	7.2 kg
Nominal envelope (L × W × H)	400 × 350 × 300 mm
Adjacent hip spacing x	120 mm
Effective leg radius R	130 mm
Fan angle α	34°
Rotary drive	24 V BLDC, planetary reducer; 320 g
Hip drive	12 V geared motor; 30 g
Aquatic interaction surface	Flexible TPU fin
Terrestrial contact	Rigid fan frame with anti-slip covering
Static / shaft seals	Epoxy potting and nitrile O-rings / PTFE lip seals

underwater substrate contact. Their integration into the torso leaves the same six leg–fin units available for both aquatic conditions.

3 Multimodal Gait Generation

3.1 Rhythmic generation and joint convention

The gait generator coordinates the two functions of each appendage through mode-dependent mappings from six rhythmic units to twelve motor-angle commands (Fig. 5). Terrestrial and underwater bottom crawling share a mapping with active hip lifting, whereas water-surface swimming uses leg rotation at a fixed hip setting. The Hopf oscillator provides the rhythmic primitive [28]; the implementation concerns its mapping to the prismatic–rotary mechanism.

The oscillator dynamics are

$$M = \begin{bmatrix} \dot{u}_i \\ \dot{v}_i \end{bmatrix} = \begin{bmatrix} \sigma(r^2 - u_i^2 - v_i^2)u_i - \omega v_i \\ \sigma(r^2 - v_i^2 - u_i^2)v_i + \omega u_i \end{bmatrix} + \lambda \sum_j \Delta_i^j. \tag{12}$$

Here, u_i and v_i are the two states of the oscillator for leg i, σ controls radial convergence, r is the target radius, ω is angular frequency, and λ weights interleg coupling. With Δ_i^j defined as the contribution from oscillator j to oscillator i, the phase-rotation term is

$$\Delta_i^j = \begin{bmatrix} \cos\Psi_i^j & -\sin\Psi_i^j \\ \sin\Psi_i^j & \cos\Psi_i^j \end{bmatrix} \begin{bmatrix} u_j \\ v_j \end{bmatrix}. \tag{13}$$

The desired phase difference Ψ_i^j is zero within each tripod group, $\{1, 4, 5\}$ and $\{2, 3, 6\}$, and π between groups. Figures 6–8 illustrate the joint commands using unit-radius sine and cosine signals with these phase offsets.

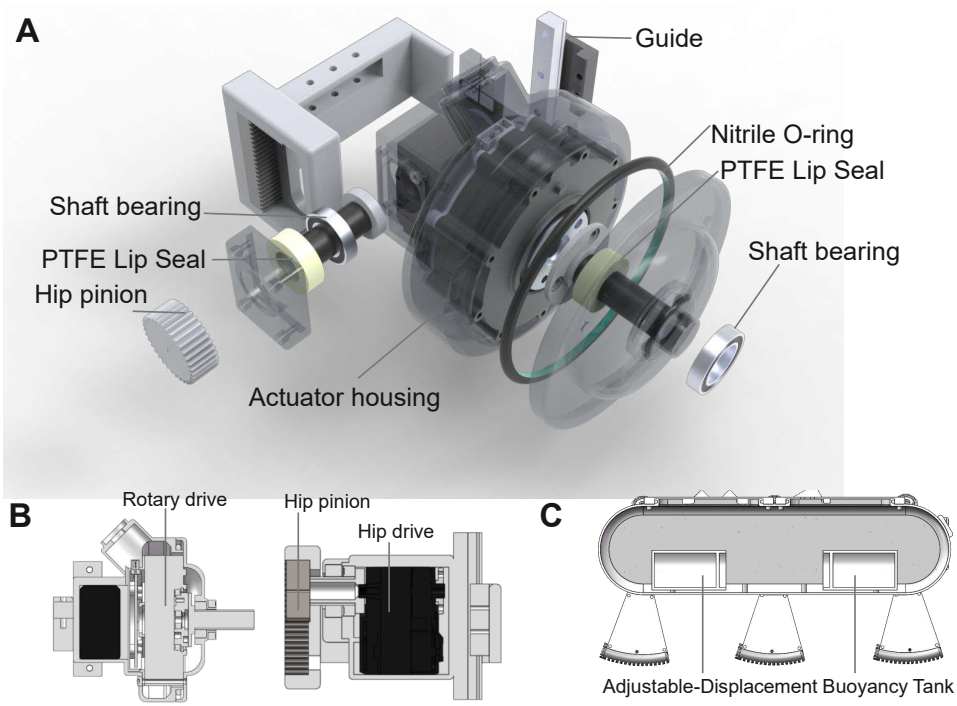


Fig. 4 Waterproof actuation and buoyancy-compartment integration. (A) Exploded assembly showing the actuator housing, hip pinion, guide, nitrile O-ring, PTFE lip seals, and shaft bearings. (B) Cross-sections through the rotary and hip drives showing their transmission and sealing arrangement. (C) Torso cross-section locating the adjustable-displacement buoyancy compartments in the lower body.

In the controller notation, θ_{i1} is the rotary leg target and θ_{i2} is the hip-drive target. This index order is opposite to the single-leg mechanical notation in Section 2: the controller's rotary target corresponds to mechanical θ_2, and its hip target corresponds to mechanical θ_1. Both controller targets are shaft angles, not linear travel. In the following mapping, k denotes the hip angular gain, whereas k_{t} denotes the length-per-radian transmission coefficient in Section 2. The figure labels "Leg" and "Hip" refer to these physical outputs.

3.2 Terrestrial and underwater bottom crawling

For the implemented phase convention, the leg uses the sine state v_i and the hip uses the positive cosine state u_i. The bounded hip mapping uses the support baseline $\theta_{2\,\mathrm{min}}$ and lift parameter $\theta_{2\,\mathrm{max}}$. The implemented crawling relation is

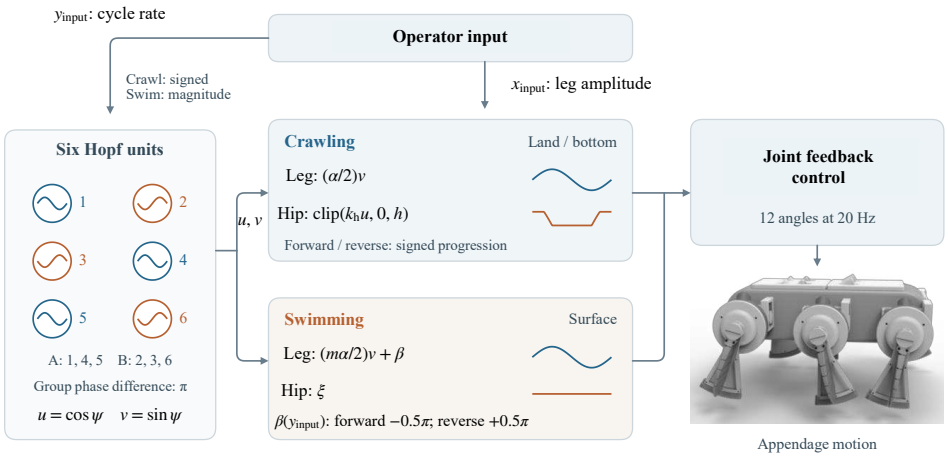


Fig. 5 Gait-generation architecture. Longitudinal input controls cycle rate and swimming sweep center; lateral input modulates leg amplitude. Six Hopf units form phase groups A={1,4,5} and B={2,3,6}. The selected mapping generates twelve joint targets at 20 Hz for joint feedback control. In the crawling block, k_{h} and h correspond to k and $\theta_{2\,\max}$ in Eq. 14.

$$\theta_{i1} = \frac{\alpha_i}{2} v_i,$$
$$\theta_{i2} = \begin{cases} \theta_{2\,\min}, & ku_i \le 0, \\ ku_i + \theta_{2\,\min}, & 0 < ku_i < \theta_{2\,\max}, \\ \theta_{2\,\max} + \theta_{2\,\min}, & ku_i \ge \theta_{2\,\max}. \end{cases} \tag{14}$$

The parameter α_i is the peak-to-peak rotary command angle. It is distinct from the geometric sector angle α, even when their numerical values coincide. The baseline is zero for the illustrated implementation. Figure 6 uses $\alpha_i = 34\pi/180$ rad, $k = 2$ rad, and $\theta_{2\,\max} = 1.2$ rad. The hip profile contains lifting, an elevated plateau, lowering, and a zero support plateau. Reversing the phase progression traverses the same sequence in the opposite direction. Expressing the branches in terms of the current oscillator state avoids undefined time intervals when the frequency is zero or changes sign.

Planned stance is assigned while the hip target is at its support baseline; all elevated targets are classified as planned swing. These are commanded states, not contact measurements. The aligned gait bars in Fig. 6 follow the waveform-and-gait-diagram convention used in hexapod control studies [29]. Underwater bottom crawling uses the same relation and tripod coordination as terrestrial crawling, including active hip lifting.

3.3 Water-surface swimming

Swimming uses periodic leg rotation while the hip remains at a selected angle. With the same state convention, the swimming relation is

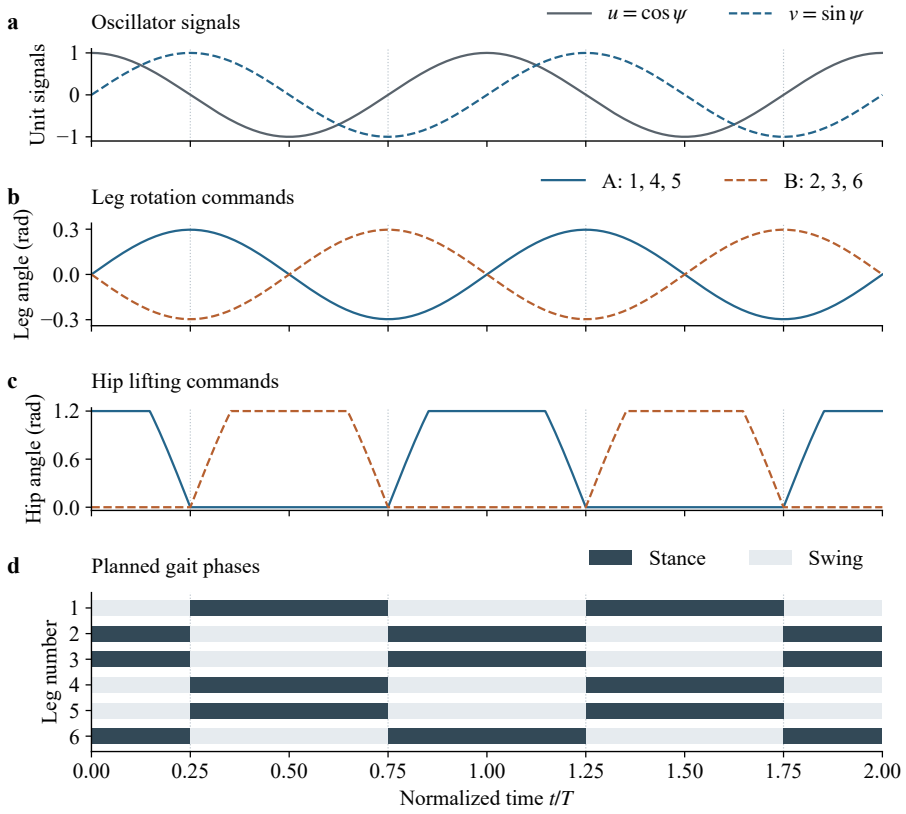


Fig. 6 Analytical crawling commands and planned gait phases. (a) Unit-limit-cycle signals for leg 1. (b,c) Leg and hip commands for the two phase groups. (d) Planned stance (dark) and swing (light) intervals. Parameters: $\alpha_i = 34\pi/180$ rad, $k = 2$ rad, $\theta_{2\,\max} = 1.2$ rad, zero hip baseline, and $\omega = 1$ rad/s ($T = 2\pi$ s).

$$\begin{aligned} \theta_{i1} &= \frac{m\alpha_i}{2} v_i + \beta_i, \\ \theta_{i2} &= \xi. \end{aligned} \tag{15}$$

Here, m scales the rotary amplitude, β_i sets the sweep center, and ξ sets the hip angle. During water-surface swimming, the leg–fin sweeps through $\pm 30°$ about its center. For $m = 1$ and unit-amplitude v_i, the peak-to-peak parameter is $\alpha_i = 60° = \pi/3$ rad. Figure 7 illustrates forward swimming with $\beta_i = -0.5\pi$ rad; its frequency and fixed hip angle $\xi = 0.2$ rad are illustrative values, as listed in Table 2.

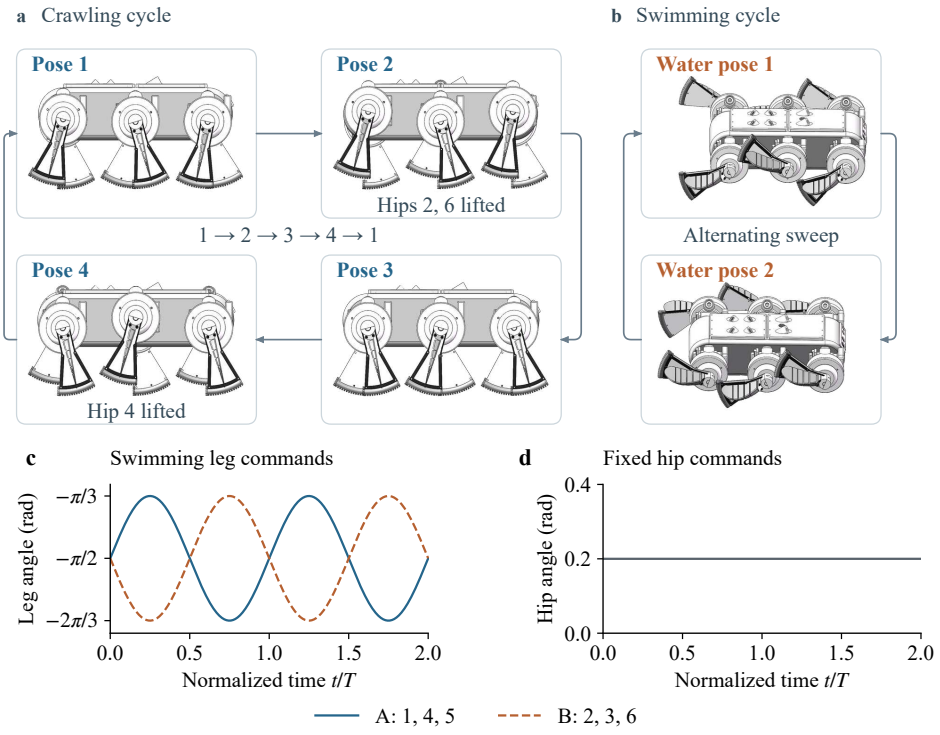


Fig. 7 Pose cycles and analytical swimming commands. (a) Crawling follows the sequence 1–2–3–4–1. Hips 2 and 6 are at maximum elevation in Pose 2, and Hip 4 in Pose 4. (b) Swimming alternates between Water poses 1 and 2. Pose spacing is schematic. (c,d) Forward-swimming leg targets and fixed hip targets for the two phase groups. The example uses $\omega = 1$ rad/s, $\alpha_i = \pi/3$ rad, $m = 1$, $\beta_i = -0.5\pi$ rad, and $\xi = 0.2$ rad. Frequency and hip angle are illustrative; the sweep is $\pm 30^\circ$.

3.4 Direction input and execution

The handheld controller supplies bounded longitudinal and lateral inputs, y_{input} and x_{input}, each between -1 and 1. For crawling, the frequency and side-dependent amplitude rules are

$$\begin{aligned} \omega &= y_{\text{input}}\omega_0, \\ \alpha_i \ (i = 1,3,5) &= \begin{cases} (1 - x_{\text{input}})\alpha_0, & x_{\text{input}} > 0, \\ \alpha_0, & x_{\text{input}} \le 0, \end{cases} \\ \alpha_i \ (i = 2,4,6) &= \begin{cases} \alpha_0, & x_{\text{input}} > 0, \\ (1 + x_{\text{input}})\alpha_0, & x_{\text{input}} \le 0. \end{cases} \end{aligned} \tag{16}$$

Positive lateral input reduces the rotary amplitude on legs 1, 3, and 5; negative input reduces it on legs 2, 4, and 6. The other side retains the default peak-to-peak amplitude α_0. Input magnitude is retained rather than normalized, allowing intermediate cycle

rates. At maximum lateral input, one side has zero rotary sweep, but its hip lifting is not automatically suppressed.

For swimming, the magnitude of longitudinal input sets a nonnegative cycle rate, and its sign selects the external angular center: $\beta_i = -0.5\pi$ rad for the forward setting and $\beta_i = +0.5\pi$ rad for the reverse setting. Zero input retains the previous center. The two settings select sweep centers separated by π rad. The swimming illustration and experiment demonstrate only forward operation; reverse swimming was not experimentally evaluated.

Joint targets are generated and transmitted every 0.05 s (20 Hz). Phase is updated by adding the angular frequency multiplied by this interval and is held when the frequency is zero. Figure 8 illustrates progression, hold, and reversal. Phase remains continuous, although abrupt changes in amplitude or mode can produce discontinuous joint targets.

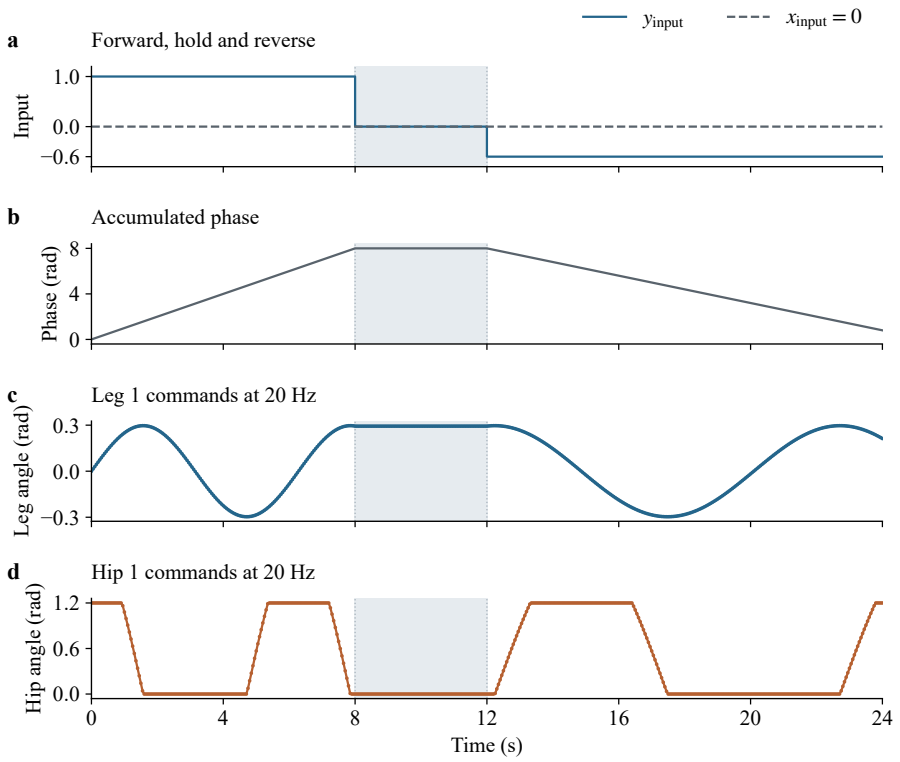


Fig. 8 Analytical online commands for leg 1. (a) Longitudinal input is 1 before 8 s, 0 from 8 to 12 s, and -0.6 thereafter; lateral input is zero. (b) Accumulated phase with $\omega_0 = 1$ rad/s. (c,d) Leg and hip targets evaluated at 20 Hz using the crawling parameters in Fig. 6. Shading marks the phase-hold interval.

The motors track the angle commands using joint feedback. The proportional–derivative torque relation is

$$\tau_{ij} = k_{\mathrm{p}}(\theta_{ij,\mathrm{d}} - \theta_{ij,\mathrm{f}}) + k_{\mathrm{d}}(\dot{\theta}_{ij,\mathrm{d}} - \dot{\theta}_{ij,\mathrm{f}}). \tag{17}$$

Here, τ_{ij} is motor torque, d and f denote desired and feedback values, and k_{p} and k_{d} are the proportional and derivative gains. Table 2 lists the implementation settings and the illustrative values used in the command figures.

Table 2 Gait implementation conventions and illustrative parameters

Parameter	Value / convention
Rhythmic units / command outputs	6 / 12
Command update interval	0.05 s (20 Hz)
Hip transmission	$k_{\mathrm{t}} = 0.04/(2\pi)$ m/rad
Phase vector, legs 1–6	[0, π, π, 0, 0, π] rad
Crawling hip baseline	0 rad
Longitudinal / lateral inputs	y_{input} / x_{input}; each in [-1, 1]
Reference angular frequency	$\omega_0 = 1$ rad/s
Crawling leg peak-to-peak angle	$34\pi/180 \approx 0.593412$ rad
Crawl Hip gain / lift	$k = 2$ rad; $\theta_{2\,\max} = 1.2$ rad
Swimming Leg sweep	$\pm 30^{\circ}$; $\alpha_i = \pi/3$ rad for $m = 1$
Swimming Hip	$\xi = 0.2$ rad
Swimming Leg center	Forward -0.5π; reverse $+0.5\pi$ rad

The gait generator automatically produces the corresponding joint commands when the operator changes the crawling or swimming map. Within a crawling cycle, the hip profile determines the lifting, elevated, lowering, and support phases.

4 Experimental Evaluation

We tested Hexplorer on flat ground, outdoor unstructured ground, at the water surface, and on an underwater substrate. The tests used the same appendages and actuators.

4.1 Experimental setup

One run was recorded for each condition. The operator supplied direction commands through a handheld controller, and the gait generator transmitted twelve joint targets at 20 Hz. The flat-ground, outdoor, and underwater bottom tests used the crawling map with active hip lifting. Surface swimming used the oscillation map with fixed hip targets. Table 3 summarizes the setup.

The four tests used the same locomotor appendages and actuator set. Before each aquatic test, the buoyancy state was preset manually for surface floating or substrate contact; the quantitative buoyancy settings were not recorded. The aquatic experiments were conducted in an inflatable pool with a water depth of 0.6 m. A fixed camera and field distance measurements supplied elapsed time and travel distance, while an

onboard inertial measurement unit (IMU) recorded yaw, pitch, and roll at a median sampling interval of approximately 17 ms.

The operator acted as an external planner by supplying direction commands through the handheld controller. Heading performance was evaluated by comparing the measured yaw angle ψ_{yaw} with the commanded heading ψ_{extern}. The heading error was defined as $\Delta\psi_{\mathrm{yaw}} = \psi_{\mathrm{yaw}} - \psi_{\mathrm{extern}}$ and characterized by its mean absolute value and variance. Pitch and roll variances were used to evaluate body-attitude stability.

Table 3 Experimental setup

Item	Setting
Prototype	Hexplorer; 7.2 kg; nominal envelope 400 × 350 × 300 mm
Locomotor hardware	Six fixed rigid-flexible leg-fin units; 12 active DOFs
Actuation	One prismatic hip and one rotary leg-fin joint per appendage
Operator interface	Conventional handheld remote controller for direction input
Command update	Twelve joint targets transmitted at 20 Hz
Hip transmission	4 cm prismatic travel per 2π rad drive rotation
Surface-swimming sweep	$\pm 30^{\circ}$ about the forward center -0.5π rad
Crawling mapping	Used on flat ground, outdoor ground, and the underwater substrate
Surface-swimming mapping	Reciprocating leg-fin rotation with a selected fixed hip setting
Buoyancy	Manually preset for surface floating or substrate contact; values not recorded
Measurements	Fixed-camera timing, field distance, and onboard IMU attitude

4.2 Flat-ground crawling

The flat-ground test used a marked path within a 3 m × 3 m rigid-floor area. High-contrast tape defined a 0.6 m-wide route with a total path length of 5 m. The robot followed straight segments and right-angle turns for 240 s (Fig. 9). The resulting mean traversal speed was 0.0208 m/s.

Figure 10 compares the measured yaw with the commanded heading and shows the pitch and roll records. The heading response time was approximately 1 s. The mean absolute heading error was 0.36°, with a variance of 0.2324 deg^2. Pitch and roll variances were 0.1286 and 0.1430 deg^2, respectively.

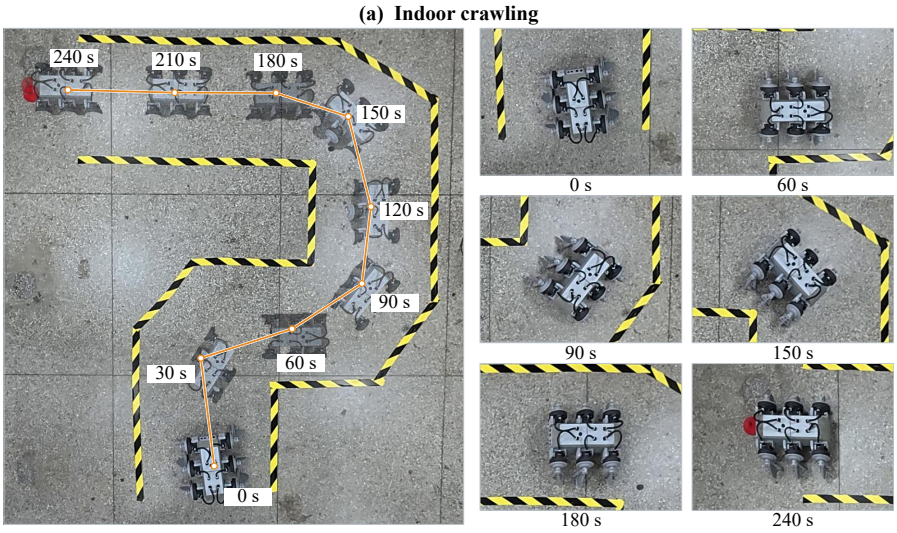


Fig. 9 Flat-ground crawling along the marked route. The overlaid path and time-stamped frames show the 240 s run.

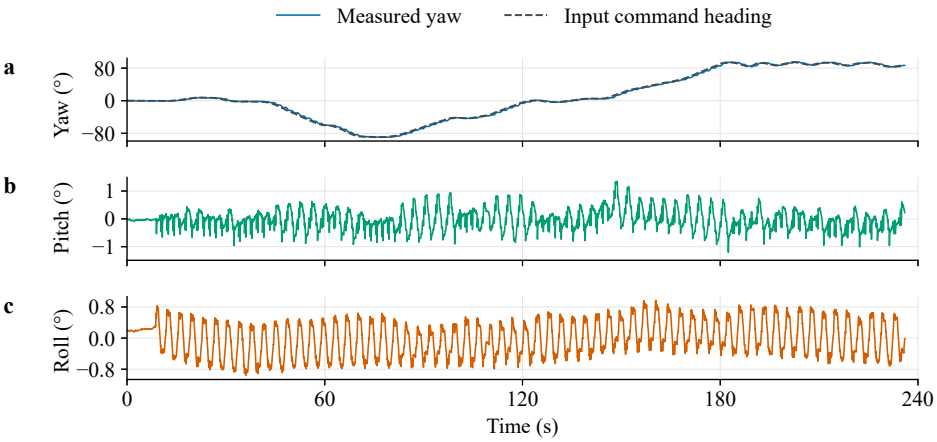


Fig. 10 Flat-ground attitude record. (a) Measured yaw and commanded heading; (b) pitch; (c) roll.

4.3 Outdoor unstructured-ground crawling

The outdoor test used soft, uneven ground with a reported slope not exceeding 2°. The robot traveled between markers 3 m apart in 120 s (Fig. 11), giving an average speed of 0.0250 m/s.

The outdoor attitude record is shown in Fig. 12. The heading response time was approximately 1 s. The mean absolute heading error was 0.61°, with a variance of

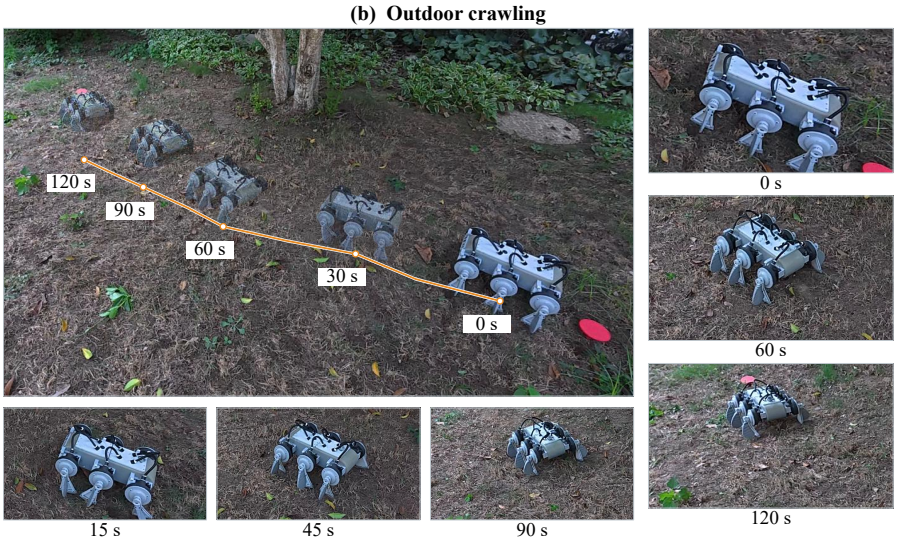


Fig. 11 Outdoor crawling on soft, uneven ground. The overlaid positions and selected frames show the 120 s run between the marked endpoints.

0.6025 deg^2. Pitch varied within approximately $\pm 5^\circ$ and roll within $\pm 4^\circ$; their variances were 2.1598 and 1.5562 deg^2, respectively.

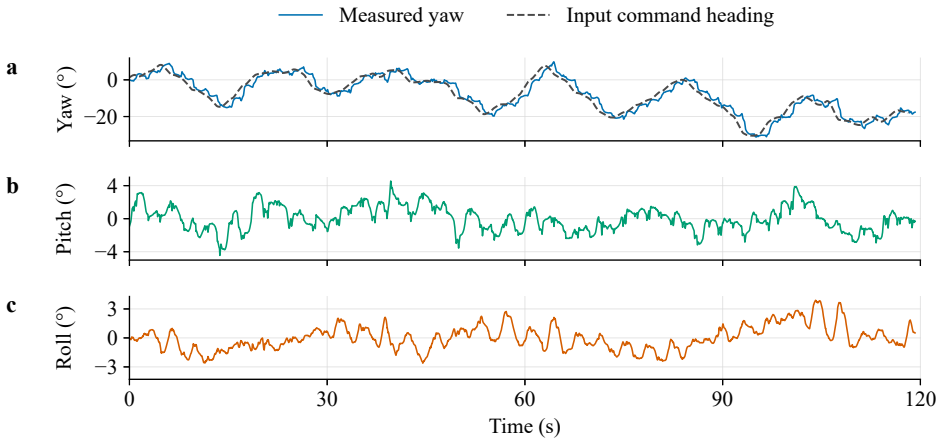


Fig. 12 Outdoor attitude record. (a) Measured yaw and commanded heading; (b) pitch; (c) roll.

4.4 Water-surface swimming

For surface swimming, the buoyancy was set to keep the robot afloat and the swimming map was selected. The robot traveled 2.5 m in 20 s in the 0.6 m-deep pool (Fig. 13), giving an average speed of 0.1250 m/s.

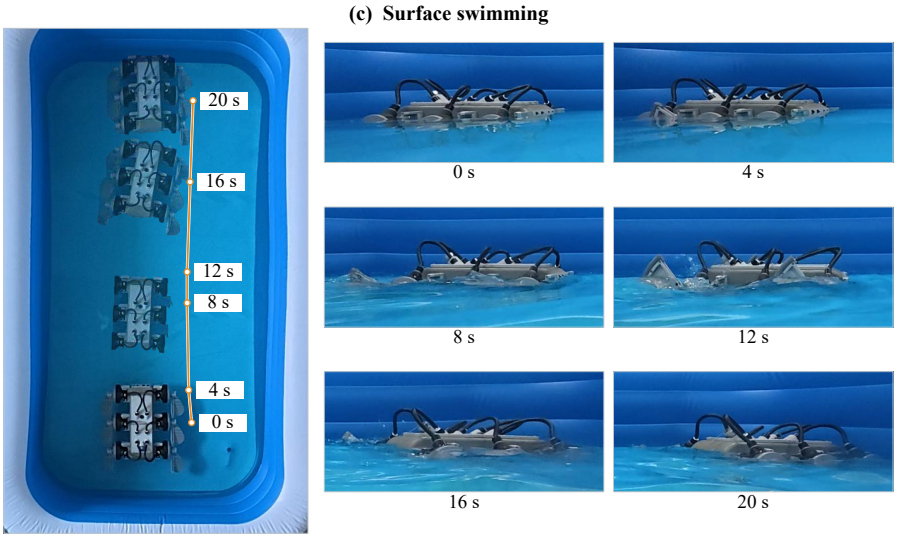


Fig. 13 Water-surface swimming over 20 s, shown by the trajectory and selected side-view frames.

The water-surface attitude record is shown in Fig. 14. The heading response time was approximately 1.5 s. The mean absolute heading error was 0.42°, with a variance of 0.0370 deg^2. Pitch and roll variances were 0.4673 and 0.4338 deg^2, respectively. Roll fluctuations decreased as the robot reached a steady swimming speed.

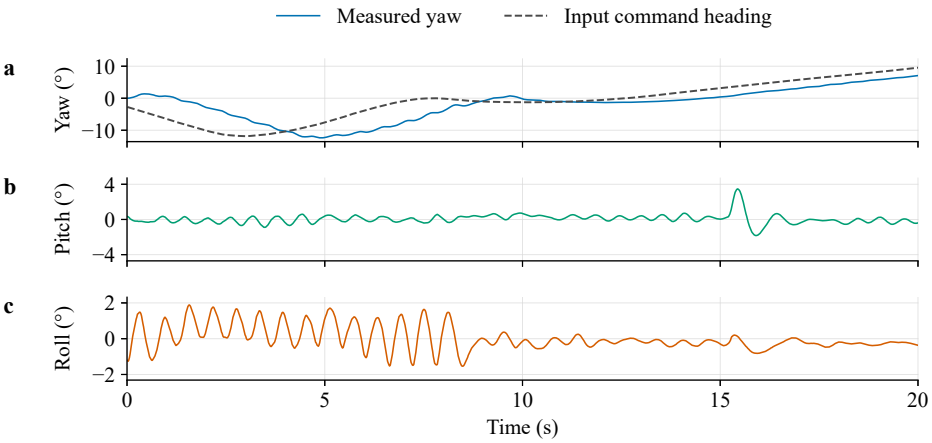


Fig. 14 Water-surface attitude record. (a) Measured yaw and commanded heading; (b) pitch; (c) roll.

4.5 Underwater bottom crawling

For bottom crawling, buoyancy was preset to maintain substrate contact. The robot used the same crawling map as on land, including active hip lifting, and covered the 2.5 m effective pool length in 70 s (Fig. 15), giving an average speed of 0.0357 m/s.

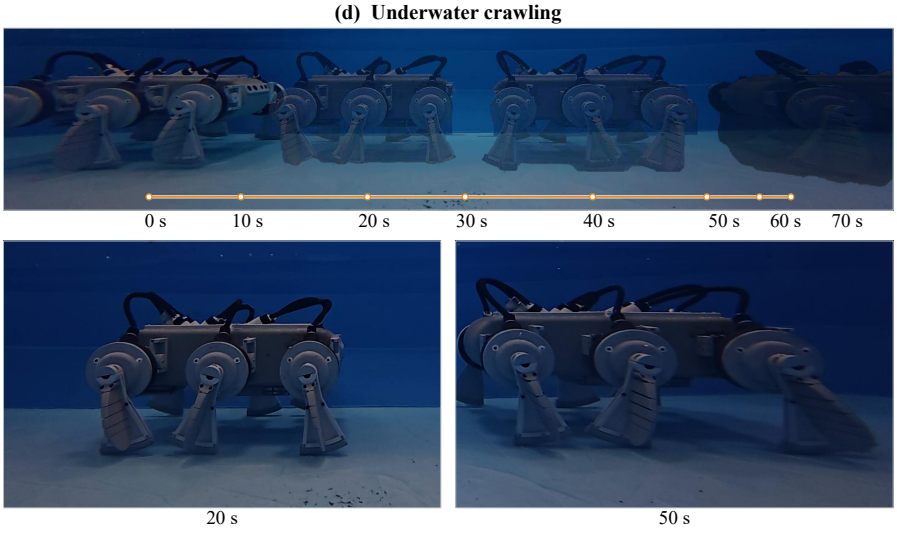


Fig. 15 Underwater bottom crawling over 70 s, shown by the overlaid positions and selected frames.

The underwater bottom-crawling attitude record is shown in Fig. 16. The heading response time was approximately 1 s. The mean absolute heading error was 0.11°, with a variance of 0.0250 deg^2. Pitch and roll variances were 0.0931 and 0.0126 deg^2, respectively, indicating smaller attitude fluctuations than in the terrestrial tests.

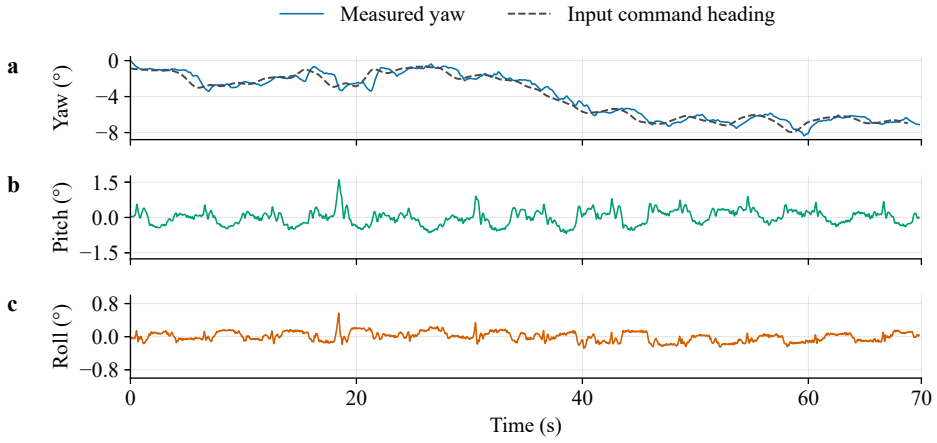


Fig. 16 Underwater bottom-crawling attitude record. (a) Measured yaw and commanded heading; (b) pitch; (c) roll.

4.6 Cross-condition summary

Table 4 summarizes heading tracking and body attitude across the four scenarios, comparing the same leg–fin mechanism and gait controller under different contact and support conditions. The heading metrics are the mean and variance of the absolute heading error; the attitude metrics are the approximate pitch and roll ranges and their respective variances.

Table 4 Heading tracking and body attitude across the experimental scenarios

Scenario	$\overline{\lvert\Delta\psi_{\text{yaw}}\rvert}$	σ_1^2	$\Delta\psi_{\text{pitch}}$	σ_2^2	$\Delta\psi_{\text{roll}}$	σ_3^2
Flat ground	0.36	0.2324	±1.5	0.1286	±1.0	0.1430
Outdoor unstructured ground	0.61	0.6025	±5.0	2.1598	±4.0	1.5562
Water surface	0.42	0.0370	±4.0	0.4673	±2.0	0.4338
Underwater bottom	0.11	0.0250	±2.0	0.0931	±0.6	0.0126

Angles and ranges are in degrees; variances are in deg^2. σ_1^2 is the variance of the absolute heading error; σ_2^2 and σ_3^2 are the pitch and roll variances.

For heading tracking, the mean absolute error ranged from 0.11° to 0.61° across the four scenarios. On flat ground, it was 0.36° as the robot followed straight segments and right-angle turns along the marked route. The outdoor unstructured-ground record had the largest mean absolute error and error variance, at 0.61° and 0.6025 deg^2, whereas bottom crawling had the smallest values, at 0.11° and 0.0250 deg^2. Heading response took approximately 1 s during crawling and 1.5 s during surface swimming, indicating a slower directional response in the swimming record. This difference may reflect the distinct interactions of oscillating fins with water and legs with a solid substrate.

For body attitude, outdoor pitch and roll varied within approximately ±5° and ±4°, with variances of 2.1598 and 1.5562 deg^2. Both exceeded the flat-ground values, consistent with larger disturbances from uneven contacts. Surface swimming showed approximate pitch and roll ranges of ±4° and ±2°, with variances of 0.4673 and 0.4338 deg^2. Bottom crawling had the lowest pitch and roll variances, at 0.0931 and 0.0126 deg^2, indicating smaller overall attitude fluctuations.

Overall, unstructured terrestrial ground posed the greatest challenge to heading tracking and attitude maintenance, while bottom crawling showed the smallest heading error and attitude variances in these records. Buoyancy assistance and substrate support may jointly reduce body disturbances underwater. These observations support operation of the mechanism and gait mappings across the four scenarios.

5 Discussion

Hexplorer performed terrestrial crawling, surface swimming, and underwater bottom crawling with the same six leg–fin units. The main design feature is the combination

of independent vertical hip motion and rotary motion in an appendage that retains its rigid frame and compliant fin across modes.

5.1 Mechanism design and locomotion coverage

The leg–fin mechanism was designed to cover terrestrial crawling, surface swimming, and underwater bottom crawling with the same appendages, without manual mechanical reconfiguration between modes. This requires each appendage to provide both substrate support and aquatic propulsion, with joint motions suited to each environment.

Hexplorer combines a rigid contact frame and a compliant TPU fin in each appendage. The frame transmits substrate loads during crawling, while the fin provides the paddling surface during swimming. A prismatic hip controls elevation independently of leg rotation, allowing the frame to be lifted during recovery and positioned for paddling. The fan radius and angle are jointly optimized within the available inter-leg spacing to balance contact sweep and reach, with terrestrial mobility as a design consideration.

Mode changes are implemented through joint motion commands. Terrestrial and underwater bottom crawling share a mapping with active hip lifting, whereas surface swimming holds the hips at a selected position and oscillates the fins. The operator selects the mapping, and the gait generator produces the corresponding joint targets. The leg–fin structure remains assembled in the same configuration throughout these modes.

Table 5 compares the reported locomotion coverage of representative robot designs. Among the examples listed, HUHR and HERO-BLUE combine swimming with bottom crawling, while AmphiHex-II combines swimming with flat-ground locomotion. The thruster-driven AUV covers swimming. Hexplorer demonstrates all four listed scenarios: flat ground, uneven ground, water-surface swimming, and underwater bottom crawling. This coverage supports the design aim of serving multiple environments with a common leg–fin mechanism.

Table 5 Terrain coverage of representative underwater robot designs

Robot design	Swimming	Flat ground	Uneven ground	Bottom crawling	Autonomous mode switching
HUHR [30]	✓	×	×	✓	✓
AmphiHex-II [21]	✓	✓	×	×	×
HERO-BLUE [24]	✓	×	×	✓	✓
Thruster-driven AUV [31]	✓	×	×	×	×
Hexplorer robot	✓	✓	✓	✓	✓

5.2 Locomotion across the tested environments

Table 6 compares whole-route average speeds across the four scenarios. Surface swimming covered 2.5 m in 20 s, giving 0.1250 m/s, compared with 0.0357 m/s for bottom

crawling, 0.0250 m/s for outdoor unstructured-ground crawling, and 0.0208 m/s for flat-ground crawling. Each average is the total travel distance divided by elapsed time. Flat-ground measurements use the marked path length, whereas the other scenarios use start-to-end travel distance; route and measurement differences therefore need to be considered in this comparison.

Table 6 Whole-route average speed comparison

Condition	Motion mode	Distance (m)	Duration (s)	Speed (m/s)
Flat ground	Terrestrial crawling	5.0	240	0.0208
Outdoor unstructured ground	Terrestrial crawling	3.0	120	0.0250
Water surface	Water-surface swimming	2.5	20	0.1250
Underwater substrate	Underwater bottom crawling	2.5	70	0.0357

Each row represents one run. Speed is distance divided by elapsed time: path length for flat-ground crawling and start-to-end travel distance for the other conditions.

To examine the initial speed evolution, the first 20 s of each run are selected for the curve comparison in Fig. 17. The two terrestrial curves remain close after the initial rise, with the outdoor record generally slightly higher. Bottom crawling reaches approximately 0.035 m/s, whereas surface swimming continues to accelerate until about 10 s and then remains near 0.15 m/s. Over 10–20 s, the sample means are 0.0245, 0.0265, 0.0355, and 0.1485 m/s for flat ground, outdoor ground, the underwater substrate, and the water surface, respectively. These local time-window averages describe the plotted records; Table 6 reports whole-route distance divided by elapsed time.

The speed curves distinguish the three locomotion modes more clearly than the two terrestrial settings. Surface swimming uses continuous fin oscillation while buoyancy supports the body; crawling alternates lifting with substrate contact. The higher swimming speed is therefore consistent with a change in propulsion and support conditions. The smaller difference between flat and outdoor crawling does not isolate a terrain effect, since the routes and contact conditions differ. The faster bottom-crawling record may reflect the reduced substrate load under buoyancy. However, reduced loading also changes available traction, while water adds resistance; the net effect cannot be assigned to friction alone.

The outdoor record showed larger pitch and roll variations than the flat-ground record, consistent with motion over uneven contacts. The underwater bottom record showed the smallest pitch and roll variances. Buoyancy and substrate support may both have contributed to the reduced angular motion.

5.3 Limitations and future work

Each condition is represented by one recorded run, so the reported speeds and attitude statistics do not quantify repeatability. The flat-ground speed uses the marked path

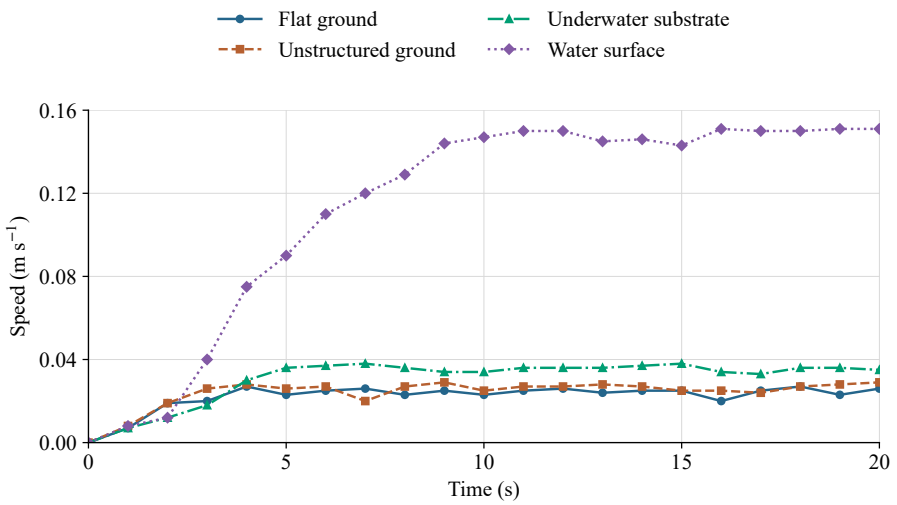


Fig. 17 Speed records for the four scenarios. The first 20 s of each run are shown. Markers indicate values at 1 s intervals, and lines connect successive points.

length, while the other speeds use start-to-end travel distance. The aquatic tests used manually preset buoyancy, without quantitative records of the settings. These differences limit comparisons between conditions. The experiments also evaluated the modes separately; continuous land–water transition and autonomous mode selection remain to be tested.

The kinematic model describes the rigid frame but does not predict fin deformation or hydrodynamic forces. Repeated tests with synchronized command, position, and attitude records would help establish locomotion consistency and heading response. Measurements of buoyancy, electrical power, and fin forces would then support analysis of the mechanical trade-offs and swimming performance. Shoreline tests are needed to determine how the robot can move between the separately demonstrated modes.

6 Conclusion

Hexplorer combines six identical prismatic–rotary leg–fin units with rigid contact frames and compliant TPU fins. The mechanism design includes joint optimization of fan radius and angle under a fixed interleg spacing. A Hopf-based gait generator drives the twelve joints, using a common crawling map on land and on an underwater substrate, and a fixed-hip oscillation map for surface swimming.

The prototype covered four locomotion scenarios with the same appendages and actuators. Average speeds in the four recorded runs were 0.0208 m/s on flat ground, 0.0250 m/s on outdoor ground, 0.1250 m/s at the water surface, and 0.0357 m/s on an underwater substrate.

Further work will quantify repeatability, power consumption, and fin forces, and evaluate continuous land–water transition.

References

[1] Hatano, M., Senzaki, M., Kawasaki, H., Takasu, C., Yamazaki, M., Hoshigami, Y.: Robots traveling on muddy terrain for sampling bottom sediment in tidal flats. Artif. Life Robot. 29(1), 155–160 (2024). https://doi.org/10.1007/s10015-023-00920-9

[2] Liu, K., Ding, M., Pan, B., Yu, P., Lu, D., Chen, S., Zhang, S., Wang, G.: A maneuverable underwater vehicle for near-seabed observation. Nat. Commun. 15(1), 10284 (2024). https://doi.org/10.1038/s41467-024-54600-8

[3] Rafeeq, M., Toha, S.F., Ahmad, S., Razib, M.A.: Locomotion Strategies for Amphibious Robots-A Review. IEEE Access 9, 26323–26342 (2021). https://doi.org/10.1109/ACCESS.2021.3057406

[4] Ijspeert, A.J.: Amphibious and Sprawling Locomotion: From Biology to Robotics and Back. Annu. Rev. Control Robot. Auton. Syst. 3(1), 173–193 (2020). https://doi.org/10.1146/annurev-control-091919-095731

[5] Xia, H., Xu, Y., Li, Z.: Hybrid actuators and their reuse methodologies for amphibious robots. Robot. Intell. Autom. 45(4), 465–480 (2025). https://doi.org/10.1108/RIA-04-2023-0051

[6] Goto, T., Nishida, K., Nakaya, K.: Internal morphology and function of paired fins in the epaulette shark, Hemiscyllium ocellatum. Ichthyol. Res. 46(3), 281–287 (1999). https://doi.org/10.1007/BF02678514

[7] Hale, M.E., Galdston, S., Arnold, B.W., Song, C.: The Water to Land Transition Submerged: Multifunctional Design of Pectoral Fins for Use in Swimming and in Association with Underwater Substrate. Integr. Comp. Biol. 62(4), 908–921 (2022). https://doi.org/10.1093/icb/icac061

[8] Quigley, Z.M.G., Blob, R.W., Kawano, S.M.: Kinematic comparisons between mudskipper fins and salamander limbs during terrestrial locomotion. J. Exp. Zool. A Ecol. Integr. Physiol. 337(6), 612–625 (2022). https://doi.org/10.1002/jez.2594

[9] Yu, J., Ding, R., Yang, Q., Tan, M., Wang, W., Zhang, J.: On a Bio-inspired Amphibious Robot Capable of Multimodal Motion. IEEE/ASME Trans. Mechatron. 17(5), 847–856 (2012). https://doi.org/10.1109/TMECH.2011.2132732

[10] Xia, M., Yin, Q., Zhu, Q., Zeng, H., Lu, Z., Luo, Z.: Toward a Track-Fin Hybrid Driven Bionic Amphibious Robot: Design, Development, and Experiments. J. Field Robot. 42(4), 1143–1165 (2025). https://doi.org/10.1002/rob.22443

[11] Zhang, H., Zhu, Y., Yang, J., Yang, C., Zhao, J.: A Bioinspired Paddle-Wheeled Leg Amphibious Robot With Environment-Adaptive Autonomously. IEEE/ASME Trans. Mechatron. 30(1), 15–26 (2025). https://doi.org/10.1109/TMECH.2024.3392553

[12] Ma, X., Wang, G., Liu, K.: Design and Optimization of a Multimode Amphibious Robot With Propeller-Leg. IEEE Trans. Robot. 38(6), 3807–3820 (2022). https://doi.org/10.1109/TRO.2022.3182880

[13] Xia, D., Yan, H., Shi, Y., Wu, J., Luo, X.: Development of a novel amphibious robot with a reusable cycloidal propulsion module. Ocean Eng. 312, 119129 (2024). https://doi.org/10.1016/j.oceaneng.2024.119129

[14] Tian, Y., Ma, S., Ohira, T., Zhang, G.: AmphiHFW: Single Actuated Amphibious Mechanism With Undulation Fin and Leg-Wheel Structure. J. Field Robot. 43(6), 4061–4075 (2026). https://doi.org/10.1002/rob.70206

[15] Zhang, S., Zhou, Y., Xu, M., Liang, X., Liu, J., Yang, J.: AmphiHex-I: Locomotory Performance in Amphibious Environments With Specially Designed Transformable Flipper Legs. IEEE/ASME Trans. Mechatron. 21(3), 1720–1731 (2016). https://doi.org/10.1109/TMECH.2015.2490074

[16] Baines, R., Freeman, S., Fish, F., Kramer-Bottiglio, R.: Variable stiffness morphing limb for amphibious legged robots inspired by chelonian environmental adaptations. Bioinspir. Biomim. 15(2), 025002 (2020). https://doi.org/10.1088/1748-3190/ab68e8

[17] Baines, R., Patiballa, S.K., Booth, J., Ramirez, L., Sipple, T., Garcia, A., Fish, F., Kramer-Bottiglio, R.: Multi-environment robotic transitions through adaptive morphogenesis. Nature 610(7931), 283–289 (2022). https://doi.org/10.1038/s41586-022-05188-w

[18] Ramirez, L.A., Baines, R., Yang, B., Kramer-Bottiglio, R.: Decreasing the Cost of Morphing in Adaptive Morphogenetic Robots. Adv. Intell. Syst. 7(9), 2401055 (2025). https://doi.org/10.1002/aisy.202401055

[19] Li, Y., Mei, S., Yin, R., Liu, C., Chen, H.: Bioinspired Origami Morphing Limbs for Amphibious Robot Locomotion. Biomimetics 11(7), 502 (2026). https://doi.org/10.3390/biomimetics11070502

[20] Wu, J., Wu, M., Chen, W., Wang, C., Xie, G.: Multimodal Soft Amphibious Robots Using Simple Plastic-Sheet-Reinforced Thin Pneumatic Actuators. IEEE Trans. Robot. 40, 1874–1889 (2024). https://doi.org/10.1109/TRO.2024.3360961

[21] Zhong, B., Zhang, S., Xu, M., Zhou, Y., Fang, T., Li, W.: On a CPG-Based Hexapod Robot: AmphiHex-II With Variable Stiffness Legs. IEEE/ASME Trans. Mechatron. 23(2), 542–551 (2018). https://doi.org/10.1109/TMECH.2018.2800776

[22] Burzynski, P., Simha, A., Kotta, Ü., Pawluszewicz, E., Sastry, S.: FLHex: a flapped-paddle hexapod for all-terrain amphibious locomotion. Bull. Pol. Acad. Sci. Tech. Sci. 69(6), e139007 (2021). https://doi.org/10.24425/bpasts.2021.139007

[23] Chen, L., Zheng, Y., Gao, D., Lu, S., Chen, B.: An amphibious tensegrity bionic mudskipper robot with asymmetric stiffness pectoral fins. Smart Mater. Struct. 35(4), 045049 (2026). https://doi.org/10.1088/1361-665X/ae5ffb

[24] Kim, T., Kim, J., Yu, S.-C.: Development of Bioinspired Multimodal Underwater Robot "HERO-BLUE" for Walking, Swimming, and Crawling. IEEE Trans. Robot. 40, 1421–1438 (2024). https://doi.org/10.1109/TRO.2024.3353040

[25] Lin, Z., Zheng, W., Zhang, J., Ou, W., Yang, C., Huang, H., Xu, W., Yang, Z., Zhou, W., Zhang, Y.: Mudskipper-inspired amphibious robotic fish enhances locomotion performance by pectoral-caudal fins coordination. Cell Rep. Phys. Sci. 4(10), 101589 (2023). https://doi.org/10.1016/j.xcrp.2023.101589

[26] Liu, A., Zhang, X., Huang, H., Xiao, F., Zhang, Z., Cui, G., Mao, B., Xu, Y., Qu, J.: An Intelligent Bionic Amphibious Turtle Robot With Visual-Tactile Fusion for Dynamic Terrain Adaptation. IEEE Trans. Robot. 41, 6345–6363 (2025). https://doi.org/10.1109/TRO.2025.3626512

[27] Zhang, Y., Cui, R., Li, H., Guo, X.: CPG-Fuzzy Heading Control for a Hexapod Robot with Arc-Shaped Blade Legs. J. Intell. Robot. Syst. 110(1), 12 (2024). https://doi.org/10.1007/s10846-023-02047-2

[28] Ijspeert, A.J.: Central pattern generators for locomotion control in animals and robots: A review. Neural Networks 21(4), 642–653 (2008). https://doi.org/10.1016/j.neunet.2008.03.014

[29] Namura, N., Nakao, H.: A central pattern generator network for simple control of gait transitions in hexapod robots based on phase reduction. Nonlinear Dynamics 113, 10105–10125 (2025). https://doi.org/10.1007/s11071-024-10773-x

[30] Zhang, G., Yan, W., Cui, R., Ma, F.: Model predictive control-based tracking controller for hybrid-driven underwater legged robot. IET Control Theory Appl. 18(18), 2646–2659 (2024). https://doi.org/10.1049/cth2.12604

[31] Gao, T., Luo, Y., Zhao, N., Gao, Y., Li, S., Fu, X., Luo, X., Shen, Y.: Design, Modeling, and MPC-Based Control of a Fully Vectored Propulsion Underwater Robot. Drones 10(2), 103 (2026). https://doi.org/10.3390/drones10020103

Statements and Declarations

Data availability: The datasets generated and analyzed during the current study are available from the corresponding author on reasonable request.

Funding: The authors declare that no funds, grants, or other support were received during the preparation of this manuscript.

Competing interests: The authors have no relevant financial or non-financial interests to disclose.

Author contributions: Ziliang Chen led the research and wrote the manuscript. Jiahong He supervised the work. Bingtuan Gao and Linlin Zhong provided guidance.